Appl. Sci. **2013**, *3*, 70-93; doi:10.3390/app3010070

OPEN ACCESS

applied sciences

ISSN 2076-3417

www.mdpi.com/journal/applsci

Review

Direct Electron Acceleration with Radially Polarized Laser Beams

Charles Varin [1,*], Stéphane Payeur [2,*], Vincent Marceau [3], Sylvain Fourmaux [2], Alexandre April [3], Bruno Schmidt [2], Pierre-Louis Fortin [3], Nicolas Thiré [2], Thomas Brabec [1], François Légaré [2], Jean-Claude Kieffer [2] and Michel Piché [3,*]

[1] Department of Physics and Centre for Photonics Research, University of Ottawa, 150 Louis Pasteur, Ottawa (Ontario) K1N 6N5, Canada; E-Mail: brabec@uottawa.ca

[2] INRS Énergie Matériaux Télécommunications, Université du Québec, 1650 boulevard Lionel-Boulet, Varennes (Québec) J3X 1S2, Canada; E-Mails: fourmaux@emt.inrs.ca (S.F.); schmidtb@emt.inrs.ca (B.S.); thire@emt.inrs.ca(N.T.); legare@emt.inrs.ca (F.L.); kieffer@emt.inrs.ca (J.-C.K.)

[3] Centre d'optique, photonique et laser, Université Laval, 2375 de la Terrasse, Québec (Québec) G1V 0A6, Canada; E-Mails: vincent.marceau.2@ulaval.ca (V.M.); alexandre.april@gmail.com (A.A.); matzrael.plf@gmail.com (P.-L.F.)

* Authors to whom correspondence should be addressed; E-Mails: cvarin@uottawa.ca (C.V.); payeur@emt.inrs.ca (S.P.); michel.piche@copl.ulaval.ca (M.P.); Tel.: +1-613-562-5757 (C.V.); +1-514-228-6900 (S.P.); +1-418-656-2753 (M.P.); Fax: +1-613-562-5190 (C.V.); +1-450-929-8102 (S.P.); +1-418-656-2623 (M.P.).

Received: 3 December 2012; in revised form: 15 January 2013 / Accepted: 16 January 2013 / Published: 30 January 2013

Abstract: In the past years, there has been a growing interest in innovative applications of radially polarized laser beams. Among them, the particular field of laser-driven electron acceleration has received much attention. Recent developments in high-power infrared laser sources at the INRS Advanced Laser Light Source (Varennes, Qc, Canada) allowed the experimental observation of a quasi-monoenergetic 23-keV electron beam produced by a radially polarized laser pulse tightly focused into a low density gas. Theoretical analyses suggest that the production of collimated attosecond electron pulses is within reach of the actual technology. Such an ultrashort electron pulse source would be a unique tool for fundamental and applied research. In this paper, we propose an overview of this emerging topic and expose some of the challenges to meet in the future.

Keywords: radially polarized beams; electron acceleration; high-power infrared sources

1. Introduction

Although the potential of lasers for particle acceleration was yet recognized in the early 1960's [1], research over the past 50 years has shown that developing an effective laser acceleration scheme is not straightforward. In the explosion-like interaction of tightly focused ultra-intense laser pulses with matter, electrons are violently expelled out of the focal region and are effectively accelerated only over short distances, typically comparable to the dominant wavelength of the pulse spectrum. Preferably, particles should be kept in phase with the intense laser field over ranges longer than the beam collimation distance. To reach this goal, a myriad of laser-light driven particle acceleration schemes have been proposed. Plasma wakefield acceleration [2,3], the most successful so far, has been proven to be reliable in producing collimated multi-MeV electron beams with per-cent-level energy spread [4–7]. Energy gains in the multi-GeV range were also reported [8,9]. Laser-wakefield accelerators, combined with a plasma-wakefield afterburner [10], have an exceptional potential for high-energy physics. However, there are also good motivations to develop sub-femtosecond electron sources at nonrelativistic energies for ultrafast electron diffraction [11–13]. Direct electron acceleration by radially polarized lasers beams (RPLBs) offers an interesting avenue [14–17]. Independent works suggest that directional and collimated attosecond electron pulses could be produced [18,19]. The experimental realization of this scheme is challenging but promising [20]. The technique could also be used for proton acceleration [21–23].

The paper is organized as follows. First, we review the characteristics of RPLBs (Section 2). Second, we present the theory behind electron acceleration in RPLBs (Section 3). Next, we discuss the special case of electron acceleration by tightly focused ultrafast radially polarized laser pulses (RPLPs) by presenting both the theory (Section 4) and experimental results (Section 5). Finally, we conclude by exposing some of the challenges to meet in the future (Section 6).

2. Radially Polarized Laser Beams

In the paraxial limit, the intensity profile of an RPLB of order p—also referred to as a TM_{p1} beam—is characterized by $p+1$ rotationally symmetric concentric rings [24,25]. There exists several ways to produce RPLBs (see Appendix A). In particular, the lowest-order RPLB (TM_{01}) is often represented as a superposition of two Hermite-Gaussian modes with orders $(0,1)$ and $(1,0)$ [26]. As the name says, the electric field oscillations of RPLBs are radially polarized (in the weak focusing limit). This feature confers to this beam family very particular properties. The most striking characteristic is the central dark intensity region that turns into a bright spot of sub-wavelength diameter under tight focusing conditions [27–29]. This behaviour is explained by the particular beam symmetry that favors a strong axial longitudinal electric field component [30].

In complex notation ($E = \mathrm{Re}[\tilde{E}\exp(j\omega_0 t + j\phi_0)]$, where ω_0 is the frequency of maximum spectral amplitude and ϕ_0 is a constant phase delay), the field components of the lowest-order RPLB can be written in the very compact form [25]:

$$\tilde{E}_r = A_0 j_2(k_0\tilde{R})\sin(2\tilde{\theta})\exp(-k_0 z_0) \quad (1a)$$

$$\tilde{E}_z = \frac{4}{3}A_0\left[j_0(k_0\tilde{R}) + j_2(k_0\tilde{R})P_2(\cos\tilde{\theta})\right]\exp(-k_0 z_0) \quad (1b)$$

$$\tilde{B}_\theta = \frac{2}{c}jA_0 j_1(k_0\tilde{R})\sin\tilde{\theta}\exp(-k_0 z_0) \quad (1c)$$

where A_0 is a normalization constant, $k_0 = \omega_0/c$ is the wave number, $j_n(k_0\tilde{R})$ is the order-n spherical Bessel function of the first kind, and $P_2(\cos\tilde{\theta}) = \frac{1}{4}[1 + 3\cos(2\tilde{\theta})]$ is the Legendre polynomial of degree 2. The complex coordinates $(\tilde{R}, \tilde{\theta})$ are defined as $\tilde{R} = [x^2 + y^2 + (z + jz_0)^2]^{1/2}$ and $\cos\tilde{\theta} = (z + jz_0)/\tilde{R}$, respectively. The confocal parameter z_0 is related to the Gaussian beam waist size w_0 by $z_0 = w_0[1 + (\frac{1}{2}k_0 w_0)^2]^{1/2}$. All other field components ($\tilde{E}_\theta$, $\tilde{B}_r$, and $\tilde{B}_z$) are zero. The beam waist corresponds to $z = 0$.

The set of Equations (1) is a rigorous closed form solution to Maxwell equations and is valid for arbitrary beam waist sizes [25,31] (see Appendix B). In the paraxial limit ($k_0 z_0 \gg 1$), the electromagnetic field components can be expanded into infinite series [30,32,33] whose leading terms are:

$$\tilde{E}_r^{(0)} = -j\frac{A_0}{k_0}\frac{r}{\tilde{q}^2}\exp\left(-\frac{jk_0 r^2}{2\tilde{q}}\right)\exp(-jk_0 z) \quad (2a)$$

$$\tilde{E}_z^{(0)} = -2\frac{A_0}{k_0^2}\frac{1}{\tilde{q}^2}\left(1 - \frac{jk_0 r^2}{2\tilde{q}}\right)\exp\left(-\frac{jk_0 r^2}{2\tilde{q}}\right)\exp(-jk_0 z) \quad (2b)$$

$$\tilde{B}_\theta^{(0)} = \tilde{E}_r^{(0)}/c \quad (2c)$$

where $\tilde{q} = z + jz_0$ is the Gaussian beam complex parameter and c the speed of light in free space. It should be noted that in the paraxial limit $z_0 \simeq z_R = k_0 w_0^2/2$, where z_R is the Rayleigh distance [34]. In the paraxial limit, the parameter A_0 is related to the peak value E_0 (in V/m) of the $\tilde{E}_r^{(0)}$ field component by $A_0 = -j(\sqrt{2}/4)k_0^3 w_0^3\exp(1/2)E_0$.

The power carried by an RPLB can be obtained through the integral of the projection of the average Poynting vector over a surface perpendicular to the beam propagation [35]. In mathematical terms it reads

$$P = \int_0^{2\pi}\int_0^{\infty}\mathbf{S}_{av}\cdot\hat{\mathbf{e}}_z r dr d\theta \quad (3a)$$

$$= \frac{1}{2\mu_0}\int_0^{2\pi}\int_0^{\infty}\mathrm{Re}\{\tilde{E}_r\tilde{B}_\theta^*\}r dr d\theta \quad (3b)$$

Accordingly, the power associated with the lowest-order RPLB is [36]

$$P = \frac{\pi A_0^2}{2\eta_0 k_0^5 z_0^3}\exp(-2k_0 z_0)[1 - 2(k_0 z_0)^2 + 2k_0 z_0\sinh(2k_0 z_0) - \cosh(2k_0 z_0)] \quad (4)$$

where $\eta_0 = \mu_0 c$ is the impedance of free space. In the paraxial limit:

$$\lim_{k_0 z_0 \gg 1} P \simeq \frac{\pi w_0^2}{4\eta_0}\exp(1)E_0^2 \quad (5)$$

In the limit where $k_0 z_0 = 0$, the power defined at Equation (4) is identically zero. It corresponds to the case where an RPLB is focused uniformly over 4π steradians [37,38]. In an ideal setup, the inward and outward energy flows would then be perfectly balanced, resulting in a null Poynting vector.

In the weak focusing limit ($k_0 z_0 \gg 1$), RPLBs appear as the characteristic doughnut-shape profile shown in Figure 1(a). In this case, most of the electric energy is concentrated in the transverse component ($W_e \propto |\mathbf{E}|^2 \simeq |E_r|^2$). Nevertheless, as the beam spot size is decreased, part of it is transferred to the longitudinal component E_z that is maximum at $r = 0$. The dark center then gradually disappears and, eventually, the longitudinal component of the electric field dominates [see Figure 1(b)–(c)]. In the limit of extreme focusing ($k_0 z_0 \to 0$), most of the electric energy is concentrated at the center of the beam that now appears as a bright symmetric spot whose diameter is smaller than the dominant laser wavelength [see Figure 1(d)]. This particular transition from paraxial to subwavelength focusing, where rotational symmetry of the beam profile is preserved, was predicted [25,28,30,33,39] and observed [27,40–43] by different authors. Because of their field symmetries and strong axial longitudinal electric field component, RPLBs are appealing for electron acceleration.

Figure 1. Transverse distribution of the average electric energy density $W_e = \epsilon_0 |\mathbf{E}|^2/2$ of a focused RPLB at beam waist. The energy density associated with the individual electric field components is shown to emphasize the contribution of the longitudinal field when the beam spot size is comparable to or below the wavelength. In (**a**) $k_0 z_0 = 350$; (**b**) $k_0 z_0 = 10$; (**c**) $k_0 z_0 = 5$; and (**d**) $k_0 z_0 = 1$. Insets show the intensity distribution (the scale is that of the corresponding transverse coordinate axis).

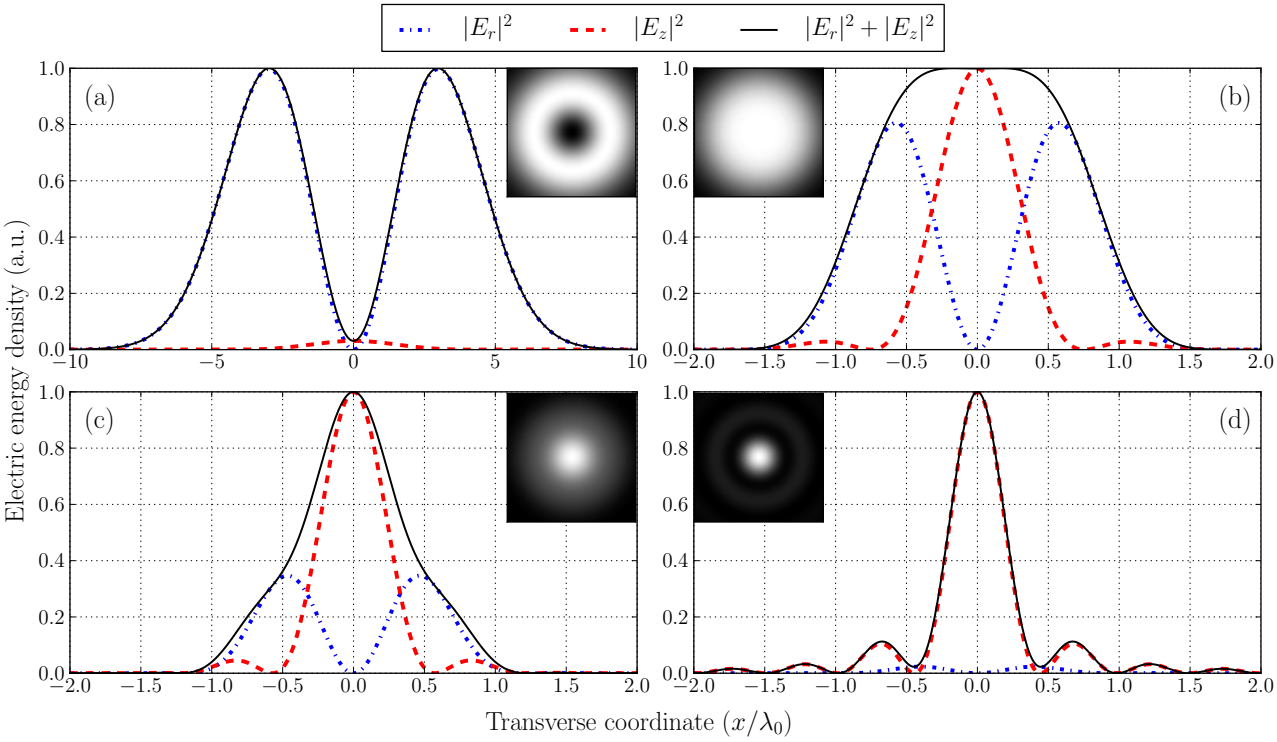

3. Electron Acceleration with Radially Polarized Laser Beams

RPLBs are the free-space analogs of the transverse-magnetic (TM) modes produced in the superconducting cavities used in conventional linear accelerators. However, acceleration with high-power lasers differs considerably from that with radio frequencies. In this section we discuss how acceleration in RPLBs proceeds and explain how attosecond electron pulses can be produced.

3.1. Free-Space Electron Acceleration in Laser Beams

The classical motion of a charged particle in a laser beam is given by the Lorentz force equation [35]:

$$\frac{d\mathbf{p}}{dt} = q\left(\mathbf{E} + \mathbf{v} \times \mathbf{B}\right) \tag{6}$$

where the particle's attributes are its mass, charge, velocity, kinetic momentum, and energy defined by the symbols m, q, $\mathbf{v}$, $\mathbf{p} = \gamma m\mathbf{v}$, and $W = \gamma mc^2$, respectively, with $\gamma = (1 - \mathbf{v}^2/c^2)^{-1/2}$. $\mathbf{E}$ and $\mathbf{B}$ are the electromagnetic field components of the laser beam [e.g., from Equations (1) or (2)]. For a non-relativistic motion in a weak harmonic electric field of angular frequency ω_0:

$$\frac{|\tilde{\mathbf{v}}|}{c} \simeq \left(\frac{q}{mc\omega_0}\right)|\tilde{\mathbf{E}}| \tag{7}$$

It is thus common to define a dimensionless parameter $a_0^2 = (q/mc\omega_0)^2 E_0^2$ whose value relative to 1 characterizes distinct regimes of particle dynamics (see Table 1).

Table 1. The three dynamical regimes associated with the motion of a charged particle in a laser beam in terms of the normalized field parameter $a_0 = (q/mc\omega_0)E_0$.

Regime	$\boldsymbol{a_0^2}$
Non-relativistic	$\ll 1$
Relativistic	~ 1
Ultra-relativistic	$\gg 1$

The non-relativistic regime is often referred to as the ponderomotive regime. Effectively, charged particles in a relatively weak laser beam ($a_0^2 \ll 1$) drift away from the high-intensity regions with an average motion that is independent of the laser polarization [44]. The mathematical form of the ponderomotive force (PF)—the net force resulting from the temporal average of the quivering particle motion associated with the rapid field oscillations—was initially proposed in the 1960's [45,46]. Relativistic ($a_0^2 \sim 1$) formulations came some 30 years later from independent authors [47–49]. In ponderomotive acceleration models, it is often assumed that the effect of the longitudinal electric field component cancels out when averaging over a full laser field cycle. For ultra-relativistic laser intensities ($a_0^2 \gg 1$), this assumption fails [16]. To effectively reveal the phase-sensitive sub-cycle dynamics that characterizes longitudinal acceleration in RPLBs, it is necessary to take into account all the field components and their oscillations, as it is done when working directly with the Lorentz force equation.

Despite the controversy that has surrounded the experimental observation of ponderomotive electron acceleration in Gaussian laser beams [50–53], the mechanism by which the particles acquire a significant (relativistic) momentum is now well understood and accepted [54]. The relativistic generalization of the original PF model [45–49] helped to explain and understand experimental observations in terms of relativistic ponderomotive scattering (RPS), where particles are expelled out of the beam focus within only a few laser cycles [55,56]. Typically, RPS proceeds in three steps. First, electrons are released by ionization (predominantly tunnel and above-threshold ionization) and accelerated toward the low-intensity regions of the laser beam by the transverse electric field component. Second, the trajectories are bent in the $\mathbf{k} \propto (\mathbf{E} \times \mathbf{B})$ direction by the magnetic field (*via* the $\mathbf{v} \times \mathbf{B}$ contribution of the Lorentz force). Third and finally, the longitudinal electric field component takes over and provides a final extra push. Although the amplitude of the longitudinal component is usually tiny ($\propto E_0\lambda_0/w_0$), including it into calculations changes the result from vanishingly small to considerable acceleration [54,55,57]. This can be explained by the fact that an electron moving longitudinally can possibly stay in phase with the longitudinal electric field over longer distances.

During RPS the electrons leave the focal region of an ultra-intense Gaussian beam with a large transverse momentum, and very few of them remain close to the beam propagation axis [51,58,59]. To limit the transverse excursion, it was proposed using a combination of a Gaussian beam and higher-order modes to create an intensity minimum at beam center that acts as a confining potential [60]. It was later shown that the use of RPLBs improves even further upon longitudinal acceleration and electron beam confinement [61,62]. The particular geometry of RPLBs forces a significant proportion of the particles to move toward the beam propagation axis and remain there while they are accelerated by the longitudinal electric field component. Authors usually refer to this phenomenon as to relativistic ponderomotive trapping (RPT) [61], in analogy to RPS where electrons are pushed toward the beam periphery.

3.2. Direct Longitudinal Electron Acceleration with Radially Polarized Laser Beams

By RPS and RPT, free electrons gain a substantial energy due to the combined action of the transverse and longitudinal electric field components. However, strong acceleration can take place at the center of RPLBs without the action of the transverse field components [16,17,63,64]. Direct longitudinal acceleration with RPLBs allows for matching the electrons with the longitudinal field oscillations and effectively offers the possibility of producing well collimated quasi-monoenergetic relativistic attosecond electron pulses [16,18,19].

The fundamental issue with longitudinal acceleration with RPLBs is the superluminous axial phase velocity. In fact, RPLBs have an axial variation of the carrier phase of $(p+2)\pi$ from $z = -\infty$ to ∞, independently of the beam spot size and pulse duration [30,39,65]. This is $(p+2)$ times that of the fundamental Gaussian beam, twice for the lowest order ($p = 0$) RPLB. This higher value of the Gouy phase shift is due to the fact that RPLBs diffract more rapidly than the fundamental Gaussian mode [66]. When considering a point of constant phase along $r = 0$, the phase velocity is

$$v_{phase} = c\left[1 - \frac{(\lambda_0/w_0)^2}{\pi^2(1 + z^2/z_R^2)}\right]^{-1} \tag{8}$$

where it was assumed that $w_0 \gg \lambda_0$ and $p = 0$, for simplicity. Because of the velocity mismatch, a particle moving in the beam will inevitably drift with respect to the carrier oscillations. Within a given time interval Δt, the net energy gain is optimal if that drift is less than half the laser wavelength, *i.e.*, if $\Delta t|v_{phase} - v_z| \lesssim \lambda_0/2$, where v_z is the particle's longitudinal velocity. During that same time interval, the particle has traveled over a distance

$$\Delta z_{dph} = \frac{\lambda_0/2}{|v_{phase}/v_z - 1|} \tag{9}$$

which defines the dephasing length. An interaction with the laser field for exactly two dephasing lengths—corresponding to a complete cycle drift—results in no acceleration, on average. For the special case of an electron with a relativistic longitudinal velocity ($v_z \simeq c$), the dephasing length is:

$$\Delta z_{dph} = \frac{\lambda_0}{2}\left[\left(\frac{\pi w_0}{\lambda_0}\right)^2 + \left(\frac{z}{w_0}\right)^2 - 1\right] \tag{10}$$

It is thus observed that around the beam waist ($z \simeq 0$), where the longitudinal field is the most intense, the distance over which a relativistic electron remains in phase with the laser field is only about the Rayleigh distance [$\Delta z_{dph} \simeq (\pi z_R)/2$]. This sets a fundamental limit on the energy that can be transferred from the laser field to particles (see also [14]).

Assuming a perfect synchronization between an electron moving along the z axis and the laser field, the maximum variation in the total electron energy from z_i to z_f is

$$\Delta W|_{z_i}^{z_f} = \mathrm{Re}\left[-e\int_{z_i}^{z_f} \tilde{E}_z(0,z)\exp(-j\phi_0)dz\right] \tag{11a}$$

$$= -ez_R E_{z0}\left\{[A(z_i) - A(z_f)]\cos\phi_0 + [B(z_i) - B(z_f)]\sin\phi_0\right\} \tag{11b}$$

where $\tilde{E}_z$ is the complex envelope of the field component given at Equation (2b). Above, $-e$ is the electron charge, $E_{z0} = [2\sqrt{2}\exp(1/2)/(k_0 w_0)]E_0$ is the amplitude of the longitudinal electric field component, $A(z) = [w_0/w(z)]^2$, and $B(z) = z_R/R(z)$. Respectively, $w(z) = w_0[1 + (z/z_R)^2]^{1/2}$ and $R(z) = z + z_R^2/z$ are the beam waist size and radius of curvature of the wavefront at z. According to Equation (11b), there are two situations where the energy gain is optimal. One is when the acceleration occurs between two axial positions where the wavefront curvature radius is minimum but of opposite sign. This happens when $[z_i, z_f] = [-z_R, z_R]$. The other situation is when acceleration takes place between two positions where the beam spot size is minimal and infinite, respectively. This corresponds to $[z_i, z_f] = [0, \pm\infty]$. For these two cases $\Delta W = ez_R E_{z0}$. This defines the following theoretical limit to the energy gain (see also [14,67,68]):

$$\Delta W_{\mathrm{lim}}[\mathrm{MeV}] \sim 31\,(P[\mathrm{TW}])^{1/2} \tag{12}$$

where $P[\mathrm{TW}]$ is the laser power in terawatts.

Different longitudinal acceleration scenarios were reported in the literature ; a selected list is given in Table 2. The first case is that of an electron that travels from $z = -\infty$ to ∞ at ultrarelativistic speed. Because of the Gouy phase, it drifts by 2π in the wave and, on average, the energy is zero. This is a

typical example that illustrates the Lawson-Woodward theorem [14]. To break the symmetry and allow for substantial electron energy gains, Scully and Zubairy [69], Esarey *et al.* [14], and Liu *et al.* [15] suggested different avenues to effectively limit the electron interaction to $-z_R \lesssim z \lesssim z_R$. However, the proposed schemes require optical materials close to the high field intensity regions. Such a configuration is inevitably limited by the destruction of the device and does not take full advantage of the high peak power delivered by actual ultraintense lasers.

As a matter of fact, material destruction—where free electrons are released due to ionization by the intense laser field—can be considered as a part of the acceleration process. A target should thus be composed preferably of a material with deeply bound inner shells so that most electrons remain bound during the rise time of the laser pulse, but released near the peak [17,19,70,71]. In that situation, electrons experience an optimal acceleration from $z \simeq 0$ to $\sim \infty$. In that range, the carrier phase shifts only by π. Here, the Lawson-Woodward theorem is not violated because the electron is initially at rest and the interaction is maintained over a semi-infinite distance. According to works by some of us, where preionized targets were considered [16,18,67], half of ΔW_{lim} comes from acceleration outside the Rayleigh zone, *i.e.*, between z_R and ∞. In this region, the longitudinal electric field is weaker than at focus but the Gouy phase evolves much more slowly (which considerably increases the dephasing time).

Table 2. Comparison between different electron acceleration scenarios in RPLBs. In the first column is the interaction range, followed by the corresponding change in energy calculated with Equation (11b), and finally a short description (scenario) with references.

$[z_i, z_f]$	$\Delta W\vert_{z_i}^{z_f}$	**Scenario**
$[-\infty, \infty]$	0	Lawson-Woodward [14]
$[-z_R, z_R]$	ΔW_{lim}	Limited interaction [14,15,69]
$[0, \infty]$	ΔW_{lim}	Single pulse [19,64,72]
$[z_R, \infty]$	$\Delta W_{\mathrm{lim}}/2$	Pump-probe [16,18,67]

The integration of Equation (11a) to get ΔW_{lim} represents ideal acceleration scenarios. Rigorous numerical simulations show that, instead, the maximum energy gain is much less unless the beam parameters are carefully optimized [67,68,73–75]. We will see in Section 4 that exceptional conditions are provided by ultrashort and tightly focused pulses.

3.3. Threshold for Sub-Cycle Acceleration and Attosecond Bunching

We now proceed with the evaluation of the threshold for sub-cycle acceleration. To account for the contribution of the longitudinal electric field component, the normalized field parameter a_0 is split into radial (a_r) and axial (a_z) components. These two new parameters are defined as follows:

$$a_r = \left(\frac{q}{mc\omega_0}\right) |\tilde{E}_r|_{peak} \tag{13a}$$

$$a_z = \left(\frac{q}{mc\omega_0}\right) |\tilde{E}_z|_{peak} \tag{13b}$$

where $|\tilde{E}_r|_{peak}$ and $|\tilde{E}_z|_{peak}$ represent the peak values of the field envelope of the radial and longitudinal components, respectively.

With Equations (1b) and (4), the threshold power corresponding to $a_z^2 = 1$ is found to be

$$P^* = \frac{9}{32}\frac{\pi}{\eta_0 (k_0 z_0)^3}\left(\frac{mc^2}{q}\right)^2 \frac{1 - 2(k_0 z_0)^2 + 2k_0 z_0 \sinh(2k_0 z_0) - \cosh(2k_0 z_0)}{|j_0(jk_0 z_0) + j_2(jk_0 z_0)|^2} \tag{14}$$

In the paraxial limit [18,67]:

$$\lim_{k_0 z_0 \gg 1} P^* \simeq \frac{\pi}{8\eta_0}\left(\frac{mc^2}{q}\right)^2 (k_0 z_0)^2 \simeq \frac{\pi^5}{2\eta_0}\left(\frac{mc^2}{q}\right)^2 \left(\frac{w_0}{\lambda_0}\right)^4 \tag{15}$$

On the other hand, the analytical evaluation of $a_r^2 = 1$, and of the corresponding threshold power, is not straightforward and best obtained numerically. Results are shown in Figure 2, where the different acceleration regimes in RPLBs are summarized.

Figure 2. Overview of electron acceleration in RPLBs. The far right of the graph corresponds to the paraxial limit, where the dynamics is dominated by the transverse electromagnetic field. In this limit, the sub-cycle longitudinal acceleration regime is reached only if the average beam power is in the PW range (see also [18,67]). Alternatively, the beam can be tightly focused to increase the peak intensity and lower the threshold down to the TWs and GWs [68,75]. The sub-cycle regime characterized by $a_z^2 > 1$ can itself be split into two sub-regimes corresponding to cases where the strength of the radial component is above threshold [Sub-cycle (1)] or not [Sub-cycle (2)].

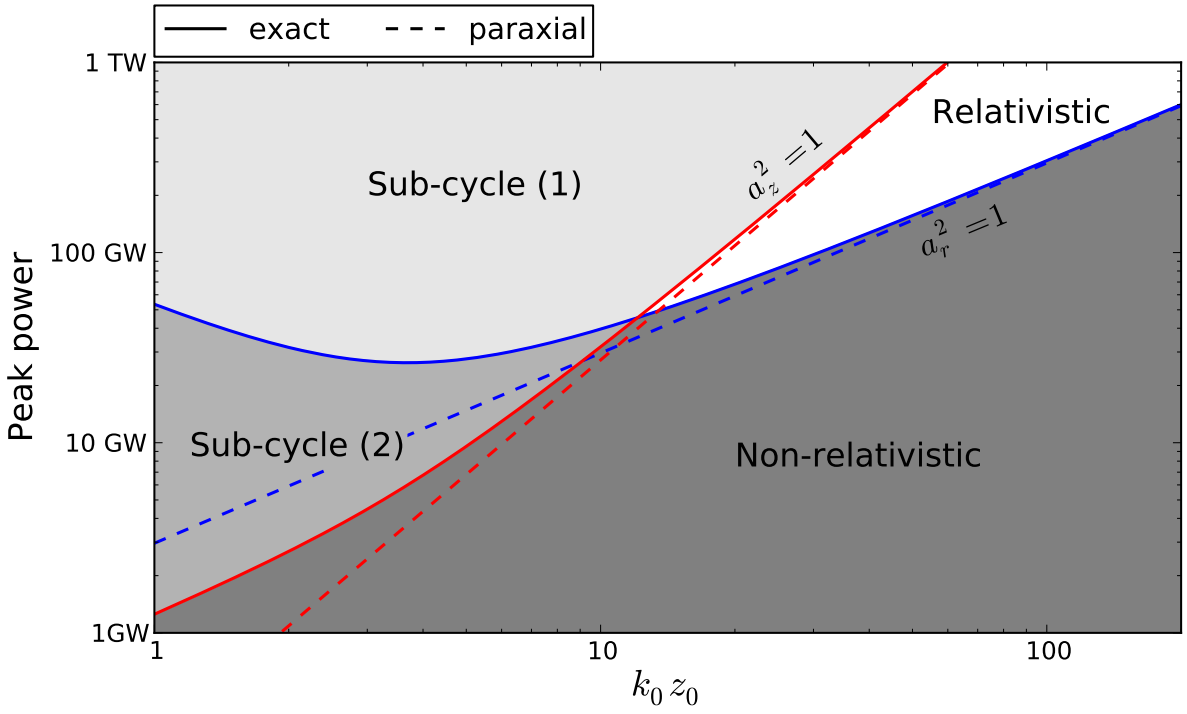

Figure 3. Single-electron model of longitudinal acceleration in a 12-fs (FWHM) RPLP ($k_0 z_0 \sim 500$ with $\lambda_0 = 800$ nm). The electron is initially at rest at $z = 0$. (**a**) At low intensity ($a_z^2 = 0.1$), the electron experiences a quasi-harmonic motion, with slightly longer excursions in accelerating half field-cycles; (**b**) At the longitudinal acceleration threshold ($a_z^2 = 1$), this phenomenon is stronger but the final kinetic energy remains relatively small (in the keV range); (**c**) Above threshold ($a_z^2 = 10$), the electron escapes the laser pulse with a relativistic longitudinal momentum. During the sub-cycle acceleration represented in (**c**), the electron stays locked to the phase of the pulse carrier.

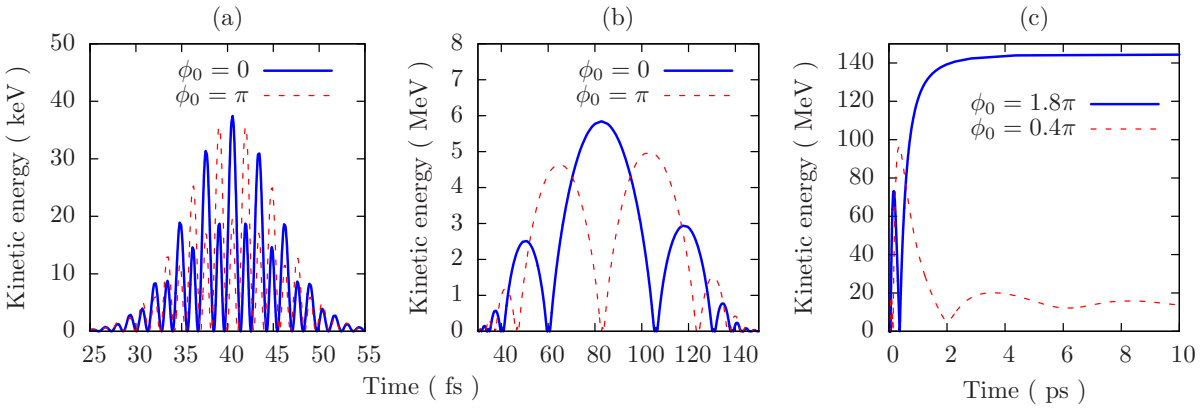

Figure 4. In the sub-cycle regime, a collection of electrons initially at rest at the waist of an ultra-intense 12-fs (FWHM) RPLP ($\lambda_0 = 800$ nm) is bunched to form an attosecond pulse. The initial electron positions (•) followed a 100-nm spherical Gaussian distribution centered at $(r, z) = (0, 0)$. Here, a magnified view reveals the extreme longitudinal compression experienced by the electrons during sub-cycle acceleration. The position of the leading edge of the accelerated electron distributions is about 6 mm away from beam waist. It was translated along z for a direct comparison of the relative durations. The size of the characters used to represent the particles gives the impression that the electron pulses are longer than they really are. For (+), we estimate that the duration along the longitudinal axis is as short as 170 zs. Simulation parameters were the following: (×) $P = 100$ TW ($k_0 z_0 \simeq 280$, $a_z^2 \simeq 4.7$), (+) $P = 1$ PW ($k_0 z_0 \simeq 850$, $a_z^2 \simeq 5.1$). The carrier phase ϕ_0 was effectively optimized for the shortest durations.

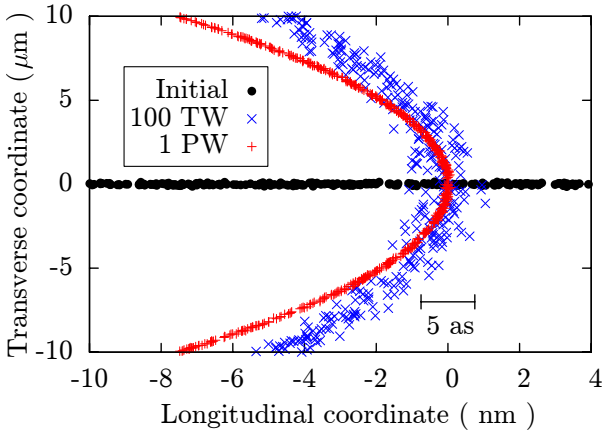

To illustrate the different regimes of longitudinal electron acceleration in RPLP, we performed a series of simulations, where the time-dependent Lorentz force equation was integrated. Results are shown in Figure 3. It is observed that above threshold ($a_z^2 \gtrsim 1$) the longitudinal electric component of the laser field is strong enough to accelerate an electron initially at rest at focus to a relativistic velocity within a half laser period. In that regime, electrons released in the same half-cycle are naturally bunched together. This is shown in Figure 4, where three-dimensional simulations were done in the single-electron approximation. More realistic simulations that include self-consistent particle interactions and ionization dynamics indicate that, in most conditions, a train of attosecond electron packets—each separated by a laser wavelength—is formed [19]. A single attosecond electron pulse could be produced if a single-cycle RPLP is used.

4. Acceleration by Ultrashort and Tightly Focused Radially Polarized Laser Pulses

Nowadays, state-of-the-art ultra-intense laser systems are able to generate terawatt laser pulses whose durations represent only a few optical cycles [76]. With high-aperture focusing systems, these ultrashort pulses can be focused on a spot of sub-wavelength dimension in the focal plane. While most theoretical studies on direct acceleration in RPLBs have limited themselves to the paraxial limit ($k_0 z_0 \gg 1$) [18,67,68], modeling the dynamics under nonparaxial and ultrashort pulse conditions is now necessary to bridge the gap between theory and current experiments (see Section 5).

A pulsed beam consists of a sum of monochromatic beams with different frequencies. In the special case of an isodiffracting pulse, each frequency component has the same wavefront curvature. A rigorous solution for the lowest-order radially polarized isodiffracting pulsed beam may therefore be obtained by taking a coherent superposition of TM_{01} beams [see Equations (1)] with different frequencies but identical confocal parameter z_0 [77]. If we weight each frequency component by the spectral amplitude function $F(\omega)$ in Fourier space and then calculate the inverse Fourier transform, we obtain the following field components in complex notation for a TM_{01} pulsed beam [75,77]:

$$\tilde{E}_r = -\frac{3jA_0 \sin 2\tilde{\theta}}{2k_0^3 \tilde{R}} \left(\frac{G_-^{(0)}}{\tilde{R}^2} - \frac{G_+^{(1)}}{c\tilde{R}} + \frac{G_-^{(2)}}{3c^2} \right) \exp(-j\omega_0 t) \tag{16a}$$

$$\tilde{E}_z = -\frac{jA_0}{k_0^3 \tilde{R}} \left[\frac{(3\cos^2\tilde{\theta} - 1)}{\tilde{R}} \left(\frac{G_-^{(0)}}{\tilde{R}} - \frac{G_+^{(1)}}{c} \right) - \frac{\sin^2\tilde{\theta}}{c^2} G_-^{(2)} \right] \exp(-j\omega_0 t) \tag{16b}$$

$$\tilde{B}_\phi = -\frac{jA_0 \sin\tilde{\theta}}{k_0^3 c^2 \tilde{R}} \left(\frac{G_-^{(1)}}{\tilde{R}} - \frac{G_+^{(2)}}{c} \right) \exp(-j\omega_0 t) \tag{16c}$$

where $G_\pm^{(n)} = \frac{\partial^n}{\partial t^n}[f(\tilde{t}_+) \pm f(\tilde{t}_-)]$, $f(t)$ is the inverse Fourier transform of the pulse spectrum $F(\omega)$ and $\tilde{t}_\pm = t \pm \tilde{R}/c + jz_0/c$. It can be verified that in the limit of a delta frequency spectrum, $F(\omega) = \delta(\omega - \omega_0)$, the fields given in Equations (1) for a TM_{01} beam of frequency ω_0 are recovered [77].

To model ultrashort pulses, a suitable frequency spectrum is the Poisson-like function [78,79]:

$$F(\omega) = 2\pi \left(\frac{s}{\omega_0} \right)^{s+1} \frac{\omega^s e^{-s\omega/\omega_0}}{\Gamma(s+1)} H(\omega) \tag{17}$$

As previously defined, ω_0 is the frequency of maximum spectral amplitude. $\Gamma(s+1)$ is the Gamma function, and $H(\omega)$ is the Heaviside step function that ensures the absence of components with negative

frequencies. The constant s is a real and positive parameter that controls the shape of the spectrum and the corresponding pulse. The inverse Fourier transform of Equation (17) is

$$f(t) = \left(1 - \frac{j\omega_0 t}{s}\right)^{-(s+1)} \tag{18}$$

which leads to exact closed-form expressions for the electromagnetic field components of the TM_{01} pulse. Note that as s increases, the width of the spectrum $F(\omega)$ decreases while the pulse duration increases. The spectrum $F(\omega)$ and the corresponding temporal profile of the E_z field component are shown in Figure 5 for different values of s.

Figure 5. (**a**) Poisson spectrum $F(\omega)$ for different values of s with $\phi_0 = 0$; (**b**) Temporal profile of the on-axis longitudinal electric field component at $z = 0$ of the corresponding TM_{01} pulsed beam with $\lambda_0 = 0.8$ μm and $k_0 z_0 = 10$.

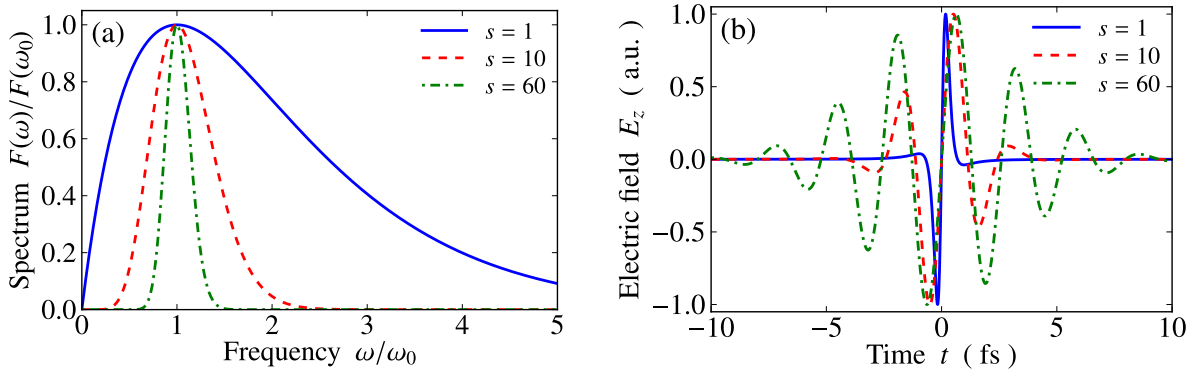

The direct acceleration of an on-axis electron by an ultrashort and nonparaxial TM_{01} pulsed beam was investigated by some of us in a recent contribution [75]. More specifically, the laser power dependence of the maximum final kinetic energy that an electron initially at rest at $r = 0$ can acquire was studied for different pulse durations and degrees of focusing. The maximum energy gain, denoted $\Delta W_{\max}$, is calculated numerically by optimizing the electron's initial position on the optical axis and the laser pulse phase such that the final kinetic energy of the particle is maximal (see also [68]).

Figure 6 shows the variation of $\Delta W_{\max}$ with the laser power for different combinations of $k_0 z_0$ and s. Figure 6(a), in which $\Delta W_{\max}$ is expressed as a fraction of the theoretical energy gain limit $\Delta W_{\lim}$ [see Equation (12)] shows that for constant values of s, the power above which significant acceleration occurs is greatly reduced as $k_0 z_0$ decreases, *i.e.*, as the focusing is made tighter. According to Figure 6(b), MeV energy gains may be reached under tight focusing conditions ($k_0 z_0 \sim 1$) with laser peak powers as low as 15 GW. In contrast, previous works based on the paraxial approximation suggested that powers three orders of magnitude higher would be required to reach MeV kinetic energies [68]. At high peak power, Figure 6(a) shows that shorter pulses yield a more efficient acceleration, with a ratio $\Delta W_{\max}/\Delta W_{\lim}$ reaching 80% for single-cycle ($s = 1$) pulses. This is mainly a consequence of the fact that shorter pulses allow the electron to move close to the pulse peak; in longer pulses, the electron is trapped and accelerated by the front edge of the pulse. As explained in [75], where additional details about the results discussed in this paragraph may be found, the data shown in Figure 6 is completely independent of the dominant wavelength λ_0 of the TM_{01} laser pulse.

Figure 6. Maximum (**a**) normalized and (**b**) absolute final energy gain of an electron initially at rest on the optical axis versus the laser pulse power for different combinations of $k_0 z_0$ and s; (**c**) A close-up on the case $k_0 z_0 = 100$ and $s = 100$ illustrates the transition from the non-relativistic (NR) to the relativistic (R) and ultra-relativistic (UR) dynamical regimes discussed in Table 1.

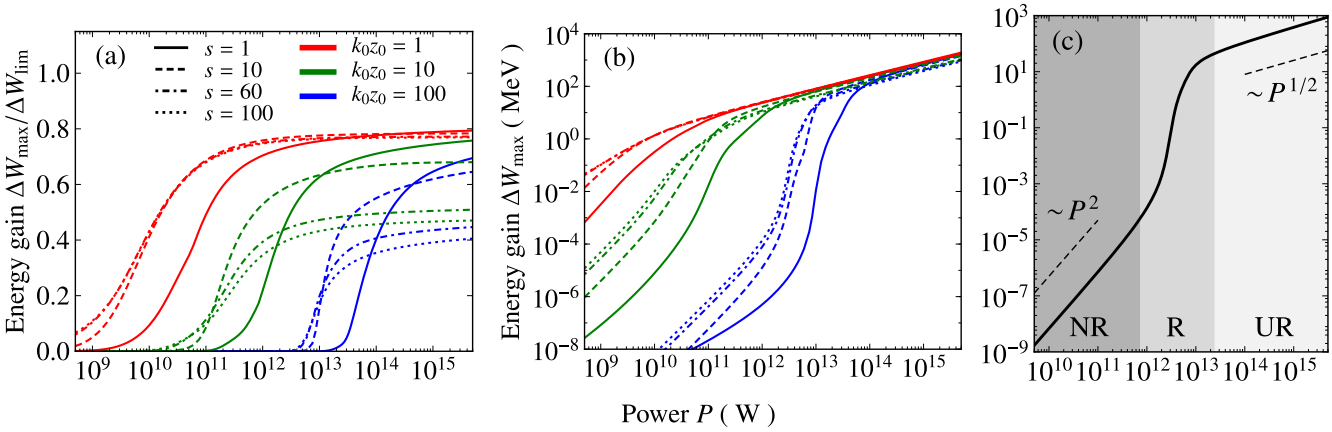

For moderately short pulses ($s \gtrsim 50$), Figure 6(b) shows well the gradual transition between the three acceleration regimes presented in Table 1. To illustrate this more clearly, the case $k_0 z_0 = 100$ and $s = 100$ is shown alone in Figure 6(c). At low laser power, $\Delta W_{\max}$ scales as P^2. This is a consequence of the ponderomotive force, which is proportional to $F_p \sim A_0^2 \sim P$ and consequently leads to an energy gain that increases as P^2. As the power is further increased, the dynamics undergoes a transition to the relativistic regime where sub-cycle acceleration begins. The maximum final kinetic energy of the electron increases rapidly since it is now allowed to copropagate with the laser pulse over longer distances. Eventually, the energy that the electron is able to extract from the pulse saturates toward a constant fraction of the theoretical energy gain limit ΔW_{lim} [see Figure 6(a)]. This marks the onset of the ultrarelativistic regime, which is characterized by the scaling relation $\Delta W_{\max} \sim P^{1/2}$, in agreement with Equation (12). For ultrashort pulses ($s \lesssim 50$), $\Delta W_{\max}$ does not scale as P^2 in the nonrelativistic regime. This shows that the ponderomotive force model is not appropriate to describe the interaction of electrons with pulses of a few-optical-cycle duration.

5. Experimental Observation of Electron Acceleration with Tightly Focused Radially Polarized Laser Beams

Recently, electron acceleration by tightly focused few-cycle RPLPs was demonstrated using an high-power infrared (IR) laser source available at the Advanced Laser Light Source (ALLS) facility (INRS, Varennes, Qc, Canada) [20]. In this section, we describe the method used to generate few-cycle RPLPs, specify the experimental conditions in which electron acceleration was observed, and present the characteristics of the accelerated electrons.

5.1. Method for Generating Tightly Focused Ultrashort RPLPs

The ALLS few-cycle IR beam line can deliver 1-mJ 15-fs pulses in the fundamental Gaussian (TEM_{00}) transverse mode at a repetition rate of 100 Hz [80]. The central wavelength is 1.8 μm and the laser pulse energy stability is of the order of 2.5% rms. The s parameter associated with these IR pulses is approximately $s = 125$.

To create the RPLB profile, we used a combination of wave plates specifically oriented in such a way that the phase of the electric field taken at any position on the beam plane is shifted by π compared to its antipodal counterpart (see Figure 7). The polarization state converter (PSC) used in the experiments is composed of 4 sections of achromatic IR half-wave plates, each having a different fast axis orientation, as shown in Figure 7(b). The created RPLB far-field mode profile, when focused by low numerical aperture (NA) optics, is shown in Figure 7(d). It is comparable to the theoretical RPLB shown in Figure 1(a), with an annular intensity profile and a minimum at the center. Weak focusing was used to image the beam with sufficient resolution. In this limit, the longitudinal field is negligible ($|E_z|^2 \ll |E_r|^2$). To reach the longitudinal acceleration threshold ($a_z^2 \sim 1$), the few-cycle RPLP was focused to a sub-wavelength focal spot with an on-axis high NA (0.7) parabolic mirror.

Figure 7. Method to generate the lowest-order RPLB. (**a**) Transverse profile of the incident linearly polarized Gaussian (TEM_{00}) beam; (**b**) The polarization state converter (PSC) composed of 4 sections of IR achromatic half-wave plates with the fast axis orientation of $0°$ (top), $+45°$ (right), $+90°$ (bottom), $-45°$ (left); (**c**) The near field beam profile and relative electric field direction at the output of the PSC; (**d**) The far field image of the weakly focused RPLB. (**a**) to (**c**) are theoretical representations while (**d**) is an experimental measurement.

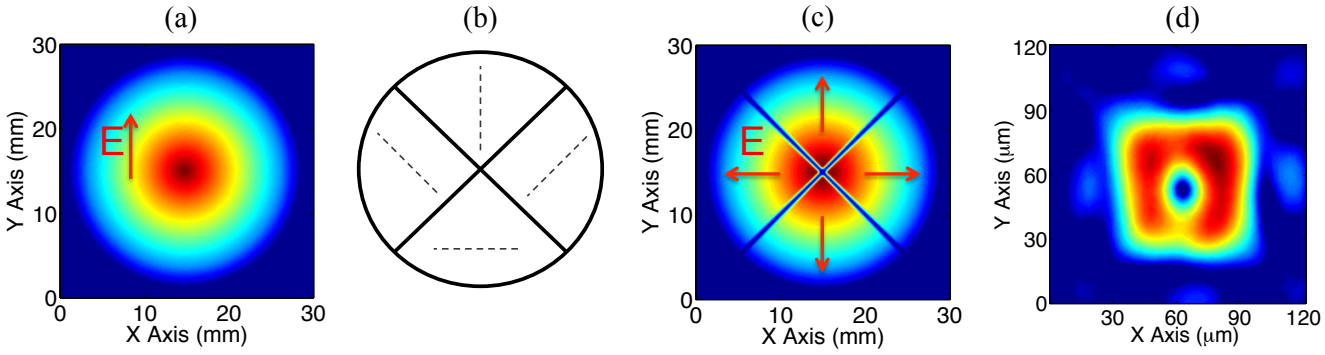

In the experimental configuration, characterization of the focal spot at high intensity is not possible by conventional methods due to the high numerical aperture and the on-axis geometry of the focusing parabola. Local surface quality of the parabola was tested and found to be better than $\lambda_0/4$ at $\lambda_0 = 675\,\mathrm{nm}$ with a diode laser source. Performances were extrapolated to 1.8 μm. The beam waist is estimated to $w_0 \approx 0.6\lambda_0$, corresponding to $k_0 z_0 \approx 8$ and a transverse beam profile somewhere in between those shown in Figure 1(b) and 1(c) ($|E_z|^2 \gtrsim |E_r|^2$). The energy measured after the parabola is 550 μJ per pulse. This results in a peak power of 36 GW and an intensity of 7.2×10^{17} W/cm^2, approximately. According to Figure 2, this corresponds to a normalized parameter $a_z^2 \simeq 1.7$. However, a comparison with Figure 6 suggests that this value of a_z^2 overestimates the real strength of the interaction. In the light of the predictions made in Section 4 and the experimental results presented below, it is most likely

that electron acceleration proceeded in the early phase of the relativistic regime where the longitudinal electric field is dominant but too weak to create attosecond electron pulses.

5.2. Electron Acceleration Measurements

For the electron acceleration experiment, the few-cycle RPLP presented in the previous section was focused into a low-density oxygen gas with a controlled pressure of 800 mTorr. According to the barrier suppression ionization model [81], up to 6 electrons per oxygen atom can be released during the interaction with the intensity mentioned above. This suggests a maximum photo-electron density of $\sim 3 \times 10^{17}$ cm^{-3} in the focal region at the peak of the laser pulse.

The experimental configuration for electron acceleration and measurement consisted of a tilted mirror, a high NA (0.7) on-axis parabola, and the electron deflector and detectors. All components were located inside a low-pressure (800 mTorr) gas chamber filled with oxygen and aligned with the focusing axis (see Figure 8). A small aperture hole was drilled in the reflective mirror to let the electron beam propagate freely to the detectors. To detect the electrons, a particle-sensitive plastic scintillator with a thin aluminum overcoat was used to convert the incoming electron beam into photons in the visible region (500 nm). These photons were then collected by a photo-mutiplier tube (PMT) to produce the correlated signal. To measure the electron distribution, the same scintillator-overcoat combination was coupled to a high dynamic range (16 bits) CCD camera.

Figure 8. RPLP electron acceleration and measurement set-up. The 25-mm diameter RPLP is reflected off a mirror placed at 45° and sent toward the focusing on-axis parabola. The resulting longitudinal field at focus is strong enough to ionize the oxygen molecules from the ambient gas (800 mTorr) and accelerate the photo-electrons along the propagation axis. The electron beam created passes through a small aperture (4 mm) in the reflecting mirror and is collected by different detectors positioned 10 cm away from the focal plane .

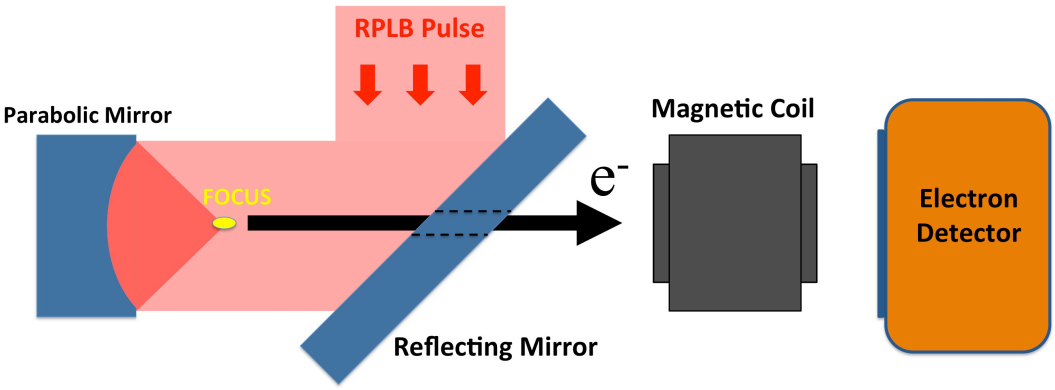

It is worth mentioning that the carrier-envelope phase of the IR pulse was not stabilized. Therefore, the carrier phase ϕ_0 was fluctuating randomly between $-\pi$ and π from shot to shot. The average transverse profile of the electron beam that propagates through the hole of the reflective mirror is shown in Figure 9(a). The measured divergence of the electron beam, from the focal plane to the detector, is 37 mrad (half-angle at 1/e). This includes probable space-charge effects and scattering.

By rotating the linear polarization before the PSC with the help of a half-wave plate, the intensity of the longitudinal field at focus can be controlled. With a vertical input polarization (90°), the output mode of the PSC has a radial polarization (TM_{01} mode) that generates a maximum longitudinal field in the focal plane. With a horizontal input polarization (0 and 180°), the output beam has an azimuthal polarization (TE_{01} mode), without a longitudinal field in the focal plane. Figure 9(b) shows the electron signal measured by the PMT while shifting gradually from a TE_{01} mode with a purely transverse electric field to a TM_{01} mode with a dominant longitudinal electric field. It is observed that the signal peaks when the effective mode approaches the ideal TM_{01} mode, where the longitudinal electric field is the strongest. On the other hand, no signal is observed with the TE_{01} or TEM_{00} mode (when removing the PSC). This is consistent with the RPLB acceleration scheme described in Section 3 where the electrons are accelerated along the propagation axis by the longitudinal electric field.

Figure 9. Experimental observation of direct longitudinal electron acceleration in tightly-focused RPLPs. (**a**) Electron beam profile averaged over 10^4 shots as observed by the camera (the circular shadow is the projected small aperture of the reflecting mirror); (**b**) Electron signal measurement from the photomultiplier tube while moving gradually from the TE_{01} mode (0° and 180°) to the TM_{01} mode (90°). The normalized longitudinal electric field intensity is also indicated; (**c**)–(**d**) Electron spectrum measurement through the magnetic coil (average of 10^4 shots); (**c**) Signal with the magnetic coil residual field of 2mT; (**d**) Signal with a magnetic field of 10mT. Both measurements confirm the production of 23-keV electrons. Figure adapted from [20].

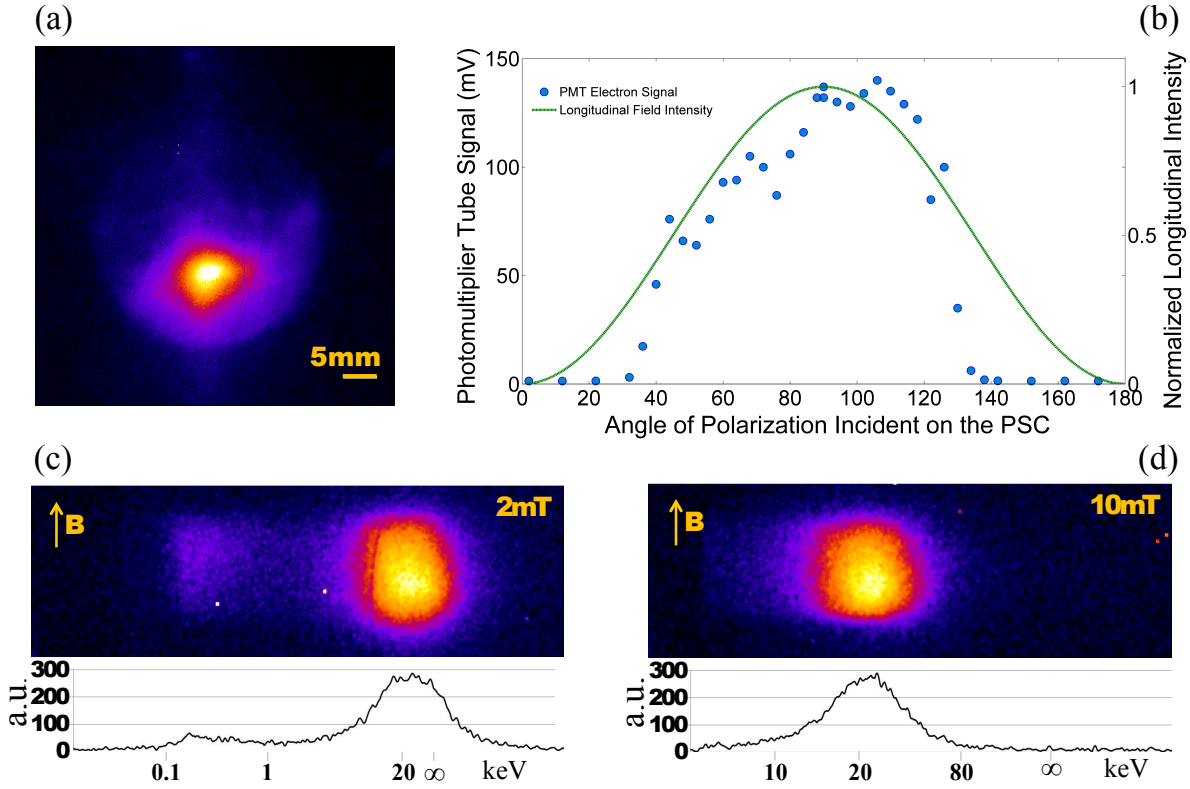

The electron energy measurement was obtained by deflecting the electron beam with the help of a magnetic coil. The calibrated magnetic field map of the coil allows us to evaluate the electron beam energy to be approximately 23 keV [Figure 9(c)–(d)]. The width of the energy distribution is estimated to be under 10% of the mean value of the energy. Electron energy losses from collisions within the gas chamber is estimated to be 0.02 keV/cm in the 15 to 25 keV range. Therefore, the influence of collisions on the overall structure of the electron energy spectrum is negligible.

A Faraday cup was used to measure about 1.2×10^6 electrons per laser shot (~ 0.2 pC per electron pulse). A linear dependence between the number of charges per shot and the pressure is observed between 50 mTorr and 1 Torr. This suggests that electron pulses with considerably more charges could be produced at higher pressures, or with solid-density targets. However, it should be noted that in these conditions space-charge effects and scattering will also be more important.

Finally, it should be stressed that the experimental set-up did not allow to resolve the temporal profile of the electron jets. However, the polarization sensitivity measured in Figure 9(b) indicates that electron emission follows the intensity of the longitudinal field. For a 23-keV electron bunch where $v_z/c \simeq 0.3$, we can thus expect a duration in the 20 fs range, close to the beam waist. We recall that non-relativistic electron pulses will broaden considerably during propagation due to velocity dispersion and space-charge effects.

6. Discussion and Conclusions

In summary, we have presented a broad overview of longitudinal electron acceleration in radially polarized laser beams and pulses. The potential of this acceleration scheme has been emphasized by several authors within the last 20 years. However, it is only until the recent developments in high-power infrared laser sources at the ALLS facility that direct acceleration of electrons at rest by the longitudinal electric component has been experimentally confirmed. The theoretical background presented here suggests that experiments were conducted just at the threshold for producing attosecond electron pulses.

The main limitation of the first ALLS experiment was the conversion efficiency of the fundamental Gaussian mode to the radially polarized mode. The actual mode converter limited the amount of energy per pulse to half a mJ. For the next set of experiments, few-mJ RPLPs with only 2 to 3 optical cycles will be produced. Avenues to produce RPLPs on the 200 TW beamline are also considered. These improvements will surely bring the future electron acceleration experiments into the sub-cycle regime.

It was shown that the static analysis presented in Section 3 provides good physical insight into the process of longitudinal electron acceleration in RPLBs. However, it does not provide accurate predictions. Dynamical analyses, like that presented in Section 4, are essential for a good understanding of the conditions in which experiments are done. The next generation of numerical analyses will have to take into account tight focusing, ultrashort pulse duration, ionization dynamics, and particle correlations. This can be done to a good extent with particle-in-cell codes (see, for example [19]). However, we emphasize the fact that modelling light-matter interaction processes in high-pressure gases and solid-density targets may require special numerical tools to correctly predict the dynamics [82].

In conclusion, attosecond electron diffraction is likely to be achieved at the INRS in a near future. Improvements to both theory and experimental procedures are still needed. Measuring and characterizing attosecond electron pulses remains, probably, the biggest challenge.

Acknowledgements

This research was supported by the Natural Sciences and Engineering Research Council of Canada (NSERC), Le Fonds de Recherche du Québec-Nature et Technologies (FRQNT), the Canadian Institute for Photonic Innovations (CIPI), the Canada Research Chairs Program, and the Ministère de l'Éducation du Québec. The ALLS facility was funded by the Canada Foundation for Innovation (CFI). The authors are also grateful to Compute Canada and the CLUMEQ consortium for computational resources.

Appendix

A. Challenges for Producing High-Power Radially Polarized Laser Beams

In laser resonators, rotational polarization symmetry is usually broken by the introduction of an optical component that is not perpendicular to the beam path, like an output mirror placed at the Brewster angle [83]. Nevertheless, if the surfaces of the optical elements inside the resonator are perpendicular to the cavity axis, the radially and azimuthally polarized transverse modes survive. Although the discrimination against the fundamental (Gaussian) and high-order modes generally leaves both the TM_{01} and TE_{01} modes, a laser cavity can be made to selectively oscillate in only one of the two by introducing a birefringent [84–86] or diffractive element [87]. Outside the cavity, the complementary TM_{01} and TE_{01} modes can be converted into each other by rotating the transverse electric field component by 90^{o} [84,85,88]. Amplification of radially polarized laser beams is also possible using specially cut Ti:sapphire crystals [89]. This offers the possibility to create dedicated ultrafast and ultra-intense laser systems tailored to specific needs.

For applications that rely on existing commercial lasers or ultra-intense laser facilities, the challenge is to develop methods to convert a linearly or circularly polarized output into radially polarized radiation with maximum conversion efficiency. The simplest approach is based on a Mach-Zehnder interferometer [90,91]. Phase masks and diffractive phase elements can also be used for better conversion efficiency [92–94]. Special polarization converters can achieve $> 99\%$ mode purity [27,95]. The beams obtained then are in good agreement with the most rigorous calculations [25,28]. However, not all these techniques are practical at the high laser intensities required for electron acceleration. Nonlinear effects, dispersion, and phase stability are important issues for potential applications of RPLBs in ultrafast science. To the best of our knowledge, these questions are not fully addressed in the literature.

B. Modelling Tightly Focused Ultrafast Laser Beams in Vacuum

The work of Lax *et al.* was one of the first to propose a systematic method to deal with the nonparaxial propagation of laser beams [32]. Following this seminal work, similar perturbative methods have also been developed for spatial corrections of various types of beams [33,96,97]. The same approach was

used in the temporal domain to solve the paraxial wave equation for ultrafast pulses [98]. Ultimately, a unification of these perturbative methods was proposed to deal with tightly focused ultrafast laser beams in a complete spatio-temporal treatment [30]. Despite its historical importance, the use of the perturbative approach is limited as it gives open-form solutions in terms of infinite series whose convergence must be ensured.

Closed-form solutions can generally be obtained *via* integral (spectral) methods: by direct Fourier and Hankel transforms [55,99,100] or through angular spectrum decomposition [47,57,101]. Very elegant solutions were also obtained using the complex source-point model [25,31]. Extending those formalisms to include both ultrashort duration and strong focusing requires extra care [77]. Final solutions should be compared against other methods, or submitted to extensive numerical tests (see, for example [102]).

References and Note

1. Shimoda, K. Proposal for an electron accelerator using an optical maser. *Appl. Opt.* **1962**, *1*, 33–35.
2. Malka, V.; Faure, J.; Gauduel, Y.A.; Lefebvre, E.; Rousse, A.; Phuoc, K.T. Principles and applications of compact laser-plasma accelerators. *Nat. Phys.* **2008**, *4*, 447–453.
3. Esarey, E.; Schroeder, C.B.; Leemans, W.P. Physics of laser-driven plasma-based electron accelerators. *Rev. Mod. Phys.* **2009**, *81*, 1229–1285.
4. Faure, J.; Glinec, Y.; Pukhov, A.; Kiselev, S.; Gordienko, S.; Lefebvre, E.; Rousseau, J.P.; Burgy, F.; Malka, V. A laser-plasma accelerator producing monoenergetic electron beams. *Nature* **2004**, *431*, 541–544.
5. Geddes, C.G.R.; Toth, C.; van Tilborg, J.; Esarey, E.; Schroeder, C.B.; Bruhwiler, D.; Nieter, C.; Cary, J.; Leemans, W.P. High-quality electron beams from a laser wakefield accelerator using plasma-channel guiding. *Nature* **2004**, *431*, 538–541.
6. Katsouleas, T. Accelerator physics: Electrons hang ten on laser wake. *Nature* **2004**, *431*, 515–516.
7. Mangles, S.P.D.; Murphy, C.D.; Najmudin, Z.; Thomas, A.G.R.; Collier, J.L.; Dangor, A.E.; Divall, E.J.; Foster, P.S.; Gallacher, J.G.; Hooker, C.J.; *et al.* Monoenergetic beams of relativistic electrons from intense laser-plasma interactions. *Nature* **2004**, *431*, 535–538.
8. Hogan, M.J.; Barnes, C.D.; Clayton, C.E.; Decker, F.J.; Deng, S.; Emma, P.; Huang, C.; Iverson, R.H.; Johnson, D.K.; Joshi, C.; *et al.* Multi-GeV energy gain in a plasma-wakefield accelerator. *Phys. Rev. Lett.* **2005**, *95*, 054802.
9. Leemans, W.P.; Nagler, B.; Gonsalves, A.J.; Toth, C.; Nakamura, K.; Geddes, C.G.R.; Esarey, E.; Schroeder, C.B.; Hooker, S.M. GeV electron beams from a centimetre-scale accelerator. *Nat. Phys.* **2006**, *2*, 696–699.
10. Blumenfeld, I.; Clayton, C.E.; Decker, F.J.; Hogan, M.J.; Huang, C.; Ischebeck, R.; Iverson, R.; Joshi, C.; Katsouleas, T.; Kirby, N.; *et al.* Energy doubling of 42-GeV electrons in a metre-scale plasma wakefield accelerator. *Nature* **2007**, *445*, 741–744.
11. Baum, P.; Zewail, A.H. 4D attosecond imaging with free electrons: Diffraction methods and potential applications. *Chem. Phys.* **2009**, *366*, 2–8.
12. Krausz, F.; Ivanov, M. Attosecond physics. *Rev. Mod. Phys.* **2009**, *81*, 163–234.
13. Zewail, A.H. Four-dimensional electron microscopy. *Science* **2010**, *328*, 187–193.

14. Esarey, E.; Sprangle, P.; Krall, J. Laser acceleration of electrons in vacuum. *Phys. Rev. E* **1995**, *52*, 5443–5453.
15. Liu, Y.; Cline, D.; He, P. Vacuum laser acceleration using a radially polarized CO_2 laser beam. *Nucl. Instrum. Methods Phys. Res. A* **1999**, *424*, 296 –303.
16. Varin, C.; Piché, M.; Porras, M.A. Acceleration of electrons from rest to GeV energies by ultrashort transverse magnetic laser pulses in free space. *Phys. Rev. E* **2005**, *71*, 026603.
17. Salamin, Y.I. Mono-energetic GeV electrons from ionization in a radially polarized laser beam. *Opt. Lett.* **2007**, *32*, 90–92.
18. Varin, C.; Piché, M. Relativistic attosecond electron pulses from a free-space laser-acceleration scheme. *Phys. Rev. E* **2006**, *74*, 045602.
19. Karmakar, A.; Pukhov, A. Collimated attosecond GeV electron bunches from ionization of high-Z material by radially polarized ultra-relativistic laser pulses. *Laser Part. Beams* **2007**, *25*, 371–377.
20. Payeur, S.; Fourmaux, S.; Schmidt, B.E.; MacLean, J.P.; Tchervenkov, C.; Legare, F.; Piche, M.; Kieffer, J.C. Generation of a beam of fast electrons by tightly focusing a radially polarized ultrashort laser pulse. *Appl. Phys. Lett.* **2012**, *101*, 41105.
21. Salamin, Y.I.; Harman, Z.; Keitel, C.H. Direct high-power laser acceleration of ions for medical applications. *Phys. Rev. Lett.* **2008**, *100*, 155004.
22. Li, J.X.; Salamin, Y.I.; Galow, B.J.; Keitel, C.H. Acceleration of proton bunches by petawatt chirped radially polarized laser pulses. *Phys. Rev. A* **2012**, *85*, 063832.
23. Liu, J.L.; Sheng, Z.M.; Zheng, J.; Liu, C.S.; Zhang, J. Proton acceleration by radially polarized chirped laser pulses. *Phys. Rev. ST Accel. Beams* **2012**, *15*, 041301.
24. Wu, G.; Lou, Q.; Zhou, J.; Dong, J.; Wei, Y. Focal shift in focused radially polarized ultrashort pulsed laser beams. *Appl. Opt.* **2007**, *46*, 6251–6255.
25. April, A. Nonparaxial TM and TE beams in free space. *Opt. Lett.* **2008**, *33*, 1563–1565.
26. Nesterov, A.V.; Niziev, V.G. Laser beams with axially symmetric polarization. *J. Phys. D* **2000**, *33*, 1817–1822.
27. Dorn, R.; Quabis, S.; Leuchs, G. Sharper focus for a radially polarized light beam. *Phys. Rev. Lett.* **2003**, *91*, 233901.
28. Quabis, S.; Dorn, R.; Eberler, M.; Glockl, O.; Leuchs, G. Focusing light to a tighter spot. *Opt. Commun.* **2000**, *179*, 1–7.
29. Youngworth, K.; Brown, T. Focusing of high numerical aperture cylindrical-vector beams. *Opt. Express* **2000**, *7*, 77–87.
30. Varin, C.; Piché, M.; Porras, M.A. Analytical calculation of the strong axial longitudinal electric field resulting from the tight focusing of an ultrafast transverse magnetic pulsed beam in free space. *J. Opt. Soc. Am. A* **2006**, *23*, 2027–2038.
31. April, A. Nonparaxial elegant Laguerre-Gaussian beams. *Opt. Lett.* **2008**, *33*, 1392–1394.
32. Lax, M.; Louisell, W.H.; McKnight, W.B. From Maxwell to paraxial wave optics. *Phys. Rev. A* **1975**, *11*, 1365–1370.
33. Salamin, Y.I. Fields of a radially polarized Gaussian laser beam beyond the paraxial approximation. *Opt. Lett.* **2006**, *31*, 2619–2621.
34. Siegman, A.E. *Lasers*; University Science: Mill Valley, CA, USA, 1986.

35. Jackson, J.D. *Classical Electrodynamics*, 3rd ed.; Wiley: New York, NY, USA, 1999.
36. April, A. Power carried by a nonparaxial TM beam. *J. Opt. Soc. Am. A* **2010**, *27*, 76–81.
37. Bokor, N.; Davidson, N. Toward a spherical spot distribution with 4π focusing of radially polarized light. *Opt. Lett.* **2004**, *29*, 1968–1970.
38. April, A.; Piché, M. 4π Focusing of TM_{01} beams under nonparaxial conditions. *Opt. Express* **2010**, *18*, 22128–22140.
39. Sheppard, C.J.R.; Saghafi, S. Transverse-electric and transverse-magnetic beam modes beyond the paraxial approximation. *Opt. Lett.* **1999**, *24*, 1543–1545.
40. Novotny, L.; Beversluis, M.R.; Youngworth, K.S.; Brown, T.G. Longitudinal field modes probed by single molecules. *Phys. Rev. Lett.* **2001**, *86*, 5251–5254.
41. Stadler, J.; Stanciu, C.; Stupperich, C.; Meixner, A.J. Tighter focusing with a parabolic mirror. *Opt. Lett.* **2008**, *33*, 681–683.
42. Imai, R.; Kanda, N.; Higuchi, T.; Zheng, Z.; Konishi, K.; Kuwata-Gonokami, M. Terahertz vector beam generation using segmented nonlinear optical crystals with threefold rotational symmetry. *Opt. Express* **2012**, *20*, 21896–21904.
43. Winnerl, S.; Hubrich, R.; Mittendorff, M.; Schneider, H.; Helm, M. Universal phase relation between longitudinal and transverse fields observed in focused terahertz beams. *New J. Phys.* **2012**, *14*, 103049.
44. Boot, H.A.H.; Harvie, R.B.R.S. Charged particles in a non-uniform radio-frequency field. *Nature (London)* **1957**, *180*, 1187.
45. Kibble, T.W.B. Mutual refraction of electrons and photons. *Phys. Rev.* **1966**, *150*, 1060–1069.
46. Kibble, T.W.B. Refraction of electron beams by intense electromagnetic waves. *Phys. Rev. Lett.* **1966**, *16*, 1054–1056.
47. Quesnel, B.; Mora, P. Theory and simulation of the interaction of ultraintense laser pulses with electrons in vacuum. *Phys. Rev. E* **1998**, *58*, 3719–3732.
48. Startsev, E.A.; McKinstrie, C.J. Multiple scale derivation of the relativistic ponderomotive force. *Phys. Rev. E* **1997**, *55*, 7527–7535.
49. Bauer, D.; Mulser, P.; Steeb, W.H. Relativistic ponderomotive force, uphill acceleration, and transition to chaos. *Phys. Rev. Lett.* **1995**, *75*, 4622–4625.
50. Lefebvre, E.; Malka, G.; Miquel, J.L. Reply to comment on 'Experimental observation of electrons accelerated in vacuum to relativistic energies by a high-intensity laser'. *Phys. Rev. Lett.* **1998**, *80*, 1352.
51. Malka, G.; Lefebvre, E.; Miquel, J.L. Experimental observation of electrons accelerated in vacuum to relativistic energies by a high-intensity laser. *Phys. Rev. Lett.* **1997**, *78*, 3314–3317.
52. McDonald, K.T. Comment on 'experimental observation of electrons accelerated in vacuum to relativistic energies by a high-intensity laser'. *Phys. Rev. Lett.* **1998**, *80*, 1350.
53. Mora, P.; Quesnel, B. Comment on 'experimental observation of electrons accelerated in vacuum to relativistic energies by a high-intensity laser'. *Phys. Rev. Lett.* **1998**, *80*, 1351.
54. Hora, H.; Hoelss, M.; Scheid, W.; Wang, J.W.; Ho, Y.K.; Osman, F.; Castillo, R. Principle of high accuracy for the nonlinear theory of the acceleration of electrons in a vacuum by lasers at relativistic intensities. *Laser Part. Beams* **2000**, *18*, 135.

55. Hartemann, F.V.; van Meter, J.R.; Troha, A.L.; Landahl, E.C.; Luhmann, N.C., Jr.; Baldis, H.A.; Gupta, A.; Kerman, A.K. Three-dimensional relativistic electron scattering in an ultrahigh-intensity laser focus. *Phys. Rev. E* **1998**, *58*, 5001–5012.
56. Hartemann, F.V.; Fochs, S.N.; Le Sage, G.P.; Luhmann, N.C.; Woodworth, J.G.; Perry, M.D.; Chen, Y.J.; Kerman, A.K. Nonlinear ponderomotive scattering of relativistic electrons by an intense laser field at focus. *Phys. Rev. E* **1995**, *51*, 4833–4843.
57. Cicchitelli, L.; Hora, H.; Postle, R. Longitudinal field components for laser beams in vacuum. *Phys. Rev. A* **1990**, *41*, 3727–3732.
58. Maltsev, A.; Ditmire, T. Above threshold ionization in tightly focused, strongly relativistic laser fields. *Phys. Rev. Lett.* **2003**, *90*, 053002.
59. Moore, C.I.; Knauer, J.P.; Meyerhofer, D.D. Observation of the transition from Thomson to Compton scattering in multiphoton interactions with low-energy electrons. *Phys. Rev. Lett.* **1995**, *74*, 2439–2442.
60. Stupakov, G.V.; Zolotorev, M.S. Ponderomotive laser acceleration and focusing in vacuum for generation of attosecond electron bunches. *Phys. Rev. Lett.* **2001**, *86*, 5274–5277.
61. Kong, Q.; Miyazaki, S.; Kawata, S.; Miyauchi, K.; Nakajima, K.; Masuda, S.; Miyanaga, N.; Ho, Y.K. Electron bunch acceleration and trapping by the ponderomotive force of an intense short-pulse laser. *Phys. Plasmas* **2003**, *10*, 4605–4608.
62. Kong, Q.; Miyazaki, S.; Kawata, S.; Miyauchi, K.; Sakai, K.; Ho, Y.K.; Nakajima, K.; Miyanaga, N.; Limpouch, J.; Andreev, A.A. Electron bunch trapping and compression by an intense focused pulse laser. *Phys. Rev. E* **2004**, *69*, 056502.
63. Varin, C.; Piché, M. Acceleration of ultra-relativistic electrons using high-intensity TM_{01} laser beams. *Appl. Phys. B* **2002**, *74*, S83–S88.
64. Salamin, Y.I. Electron acceleration from rest in vacuum by an axicon Gaussian laser beam. *Phys. Rev. A* **2006**, *73*, 043402.
65. Sheppard, C.J.R.; Saghafi, S. Electromagnetic Gaussian beams beyond the paraxial approximation. *J. Opt. Soc. Am. A* **1999**, *16*, 1381–1386.
66. Freiberg, R.J.; Halsted, A.S. Properties of low order transverse modes in argon ion lasers. *Appl. Opt.* **1969**, *8*, 355–362.
67. Fortin, P.L.; Piché, M.; Varin, C. Direct-field electron acceleration with ultrafast radially polarized laser beams: scaling laws and optimization. *J. Phys. B* **2010**, *43*, 025401.
68. Wong, L.J.; Kärtner, F.X. Direct acceleration of an electron in infinite vacuum by a pulsed radially-polarized laser beam. *Opt. Express* **2010**, *18*, 25035–25051.
69. Scully, M.O.; Zubairy, M.S. Simple laser accelerator: Optics and particle dynamics. *Phys. Rev. A* **1991**, *44*, 2656–2663.
70. Singh, K.P.; Kumar, M. Electron acceleration by a radially polarized laser pulse during ionization of low density gases. *Phys. Rev. ST Accel. Beams* **2011**, *14*, 30401.
71. The idea was initially proposed by Moore *et al.* [103] and by Hu and Starace [104] for ponderomotive acceleration in Gaussian beams.
72. Bochkarev, S.G.; Popov, K.I.; Bychenkov, V.Y. Vacuum electron acceleration by a tightly focused, radially polarized, relativistically strong laser pulse. *Plasma Phys. Rep.* **2011**, *37*, 603–614.

73. Wong, L.J.; Kärtner, F.X. Two-color-laser-driven direct electron acceleration in infinite vacuum. *Opt. Lett.* **2011**, *36*, 957–959.
74. Malav, H.; Maheshwari, K.P.; Senecha, V. Analytical and numerical investigation of the effect of pulse shape of intense, few-cycles TM_{01} laser on the acceleration of charged particles. *Ind. J. Pure & Appl. Phys.* **2011**, *49*, 251–256.
75. Marceau, V.; April, A.; Piché, M. Electron acceleration driven by ultrashort and nonparaxial radially polarized laser pulses. *Opt. Lett.* **2012**, *37*, 2442–2444.
76. Mourou, G.A.; Tajima, T.; Bulanov, S.V. Optics in the relativistic regime. *Rev. Mod. Phys.* **2006**, *78*, 309–371.
77. April, A. Ultrashort, Strongly Focused Laser Pulses in Free Space. In *Coherence and Ultrashort Pulse Laser Emission*; Duarte, F.J., Ed.; InTech: New York, NY, USA, 2010; pp. 355–382.
78. Caron, C.F.R.; Potvliege, R.M. Free-space propagation of ultrashort pulses: Space-time couplings in Gaussian pulse beams. *J. Mod. Opt.* **1999**, *46*, 1881–1891.
79. Feng, S.; Winful, H.G. Spatiotemporal structure of isodiffracting ultrashort electromagnetic pulses. *Phys. Rev. E* **2000**, *61*, 862–873.
80. Schmidt, B.E.; Shiner, A.D.; Lassonde, P.; Kieffer, J.C.; Corkum, P.B.; Villeneuve, D.M.; Légaré, F. CEP stable 1.6 cycle laser pulses at 1.8 μm. *Opt. Express* **2011**, *19*, 6858–6864.
81. Augst, S.; Meyerhofer, D.D.; Strickland, D.; Chin, S.L. Laser ionization of noble gases by Coulomb-barrier suppression. *J. Opt. Soc. Am. B* **1991**, *8*, 858–867.
82. Varin, C.; Peltz, C.; Brabec, T.; Fennel, T. Attosecond plasma wave dynamics in laser-driven cluster nanoplasmas. *Phys. Rev. Lett.* **2012**, *108*, 175007.
83. Tovar, A.A. Production and propagation of cylindrically polarized Laguerre-Gaussian laser beams. *J. Opt. Soc. Am. A* **1998**, *15*, 2705–2711.
84. Pohl, D. Operation of a ruby laser in the purely transverse electric mode TE_{01}. *Appl. Phys. Lett.* **1972**, *20*, 266–267.
85. Meier, M.; Romano, V.; Feurer, T. Material processing with pulsed radially and azimuthally polarized laser radiation. *Appl. Phys. A* **2007**, *86*, 329–334.
86. Moshe, I.; Jackel, S.; Meir, A. Production of radially or azimuthally polarized beams in solid-state lasers and the elimination of thermally induced birefringence effects. *Opt. Lett.* **2003**, *28*, 807–809.
87. Nesterov, A.V.; Niziev, V.G.; Yakunin, V.P. Generation of high-power radially polarized beam. *J. Phys. D: Appl. Phys.* **1999**, *32*, 2871–2875.
88. Niziev, V.G.; Nesterov, A.V. Influence of beam polarization on laser cutting efficiency. *J. Phys. D: Appl. Phys.* **1999**, *32*, 1455–1461.
89. Kawauchi, H.; Kozawa, Y.; Sato, S. Generation of radially polarized Ti:sapphire laser beam using a c-cut crystal. *Opt. Lett.* **2008**, *33*, 1984–1986.
90. Tidwell, S.; Ford, D.H.; Kimura, D. Generating radially polarized beams interferometrically. *Appl. Opt.* **1990**, *29*, 2234–2239.
91. Youngworth, K.S.; Brown, T.G. Inhomogenous polarization in scanning optical microscopy. *Proc. SPIE* **2000**, *3919*, 75–85.
92. Churin, E.; Hofeld, J.; Tschudi, T. Polarization configurations with singular point formed by computer generated holograms. *Opt. Commun.* **1993**, *99*, 13–17.

93. Niu, C.H.; Gu, B.Y.; Dong, B.Z.; Zhang, Y. A new method for generating axially symmetric and radially polarized beams. *J. Phys. D* **2005**, *38*, 827–832.
94. Machavariani, G.; Lumer, Y.; Moshe, I.; Meir, A.; Jackel, S. Efficient extracavity generation of radially and azimuthally polarized beams. *Opt. Lett.* **2007**, *32*, 1468–1470.
95. Bomzon, Z.; Biener, G.; Kleiner, V.; Hasman, E. Radially and azimuthally polarized beams generated by space-variant dielectric subwavelength gratings. *Opt. Lett.* **2002**, *27*, 285–287.
96. Davis, L.W. Theory of electromagnetic beams. *Phys. Rev. A* **1979**, *19*, 1177–1179.
97. Agrawal, G.P.; Lax, M. Free-space wave propagation beyond the paraxial approximation. *Phys. Rev. A* **1983**, *27*, 1693–1695.
98. Porras, M.A. Pulse correction to monochromatic light-beam propagation. *Opt. Lett.* **2001**, *26*, 44–46.
99. Carter, W.H. Anomalies in the field of a gaussian beam near focus. *Opt. Commun.* **1973**, *7*, 211–218.
100. Novotny, L.; Hecht, B. *Principles of Nano-Optics*; Cambridge University Press: New York, NY, USA, 2006.
101. Deng, D.; Guo, Q. Analytical vectorial structure of radially polarized light beams. *Opt. Lett.* **2007**, *32*, 2711–2713.
102. An der Brügge, D.; Pukhov, A. Ultrashort focused electromagnetic pulses. *Phys. Rev. E* **2009**, *79*, 016603.
103. Moore, C. I.; Ting, A.; McNaught, S. J.; Qiu, J.; Burris, H. R.; Sprangle; P. A laser-accelerator injector based on laser ionization and ponderomotive acceleration of electrons. *Phys. Rev. Lett.* **1999**, *82*, 1688-1691.
104. Hu, S. X.; Starace, A. F. GeV electrons from ultraintense laser interaction with highly charged ions. *Phys. Rev. Lett.* **2002**, *88*, 245003.